Energy Materials

Article

Impact of compaction pressure on formation and performance of garnet-based solid-state lithium batteries

Jie Zhu[1,#], Yunfan Wu[2,#], Hongyi Zhang[1], Xujia Xie[1], Yong Yang[1], Hongyu Peng[1], Xiaochun Liang[1], Qiongqiong Qi[3], Weibin Lin[3], Dong-Liang Peng[1], Laisen Wang[1,*], Jie Lin[1,*]

[1]College of Materials, State Key Laboratory for Physical Chemistry of Solid Surfaces, Fujian Key Laboratory of Surface and Interface Engineering for High Performance Materials, and Collaborative Innovation Center of Chemistry for Energy Materials, Xiamen University, Xiamen 361005, Fujian, China.
[2]State Key Laboratory of Space Power Sources, Shanghai Institute of Space Power-Sources, Shanghai 200245, China.
[3]Application Center Lab, Initial Energy Science and Technology, Xiamen 361000, Fujian, China.
[#]Authors contributed equally.

*Correspondence to: Prof. Jie Lin, College of Materials, State Key Laboratory for Physical Chemistry of Solid Surfaces, Fujian Key Laboratory of Surface and Interface Engineering for High Performance Materials, and Collaborative Innovation Center of Chemistry for Energy Materials, Xiamen University, No. 422, Siming South Road, Xiamen 361005, Fujian, China. E-mail: linjie@xmu.edu.cn; Prof. Laisen Wang, College of Materials, State Key Laboratory for Physical Chemistry of Solid Surfaces, Fujian Key Laboratory of Surface and Interface Engineering for High Performance Materials, and Collaborative Innovation Center of Chemistry for Energy Materials, Xiamen University, No. 422, Siming South Road, Xiamen 361005, Fujian, China. E-mail: wangls@xmu.edu.cn

Abstract

Compaction pressure directly determines the compactness of solid-state electrolytes (SSEs), which is crucial to affect the electrochemical performance of solid-state lithium batteries (SLBs). Herein, $Li_{6.5}La_3Zr_{1.5}Ta_{0.5}O_{12}$ (LLZTO) pellets are compacted under various pressures before sintering to study the impact of compaction pressure on the overall properties of LLZTO SSEs and their SLBs. Notably, the sample pressed at 600 MPa (LLZTO-600) exhibits the highest compactness and the highest ionic conductivity due to improved particle contact and suppressed lithium loss. Consequently, the Li|LLZTO-600|Li symmetric cell exhibits the best performance among the samples, which can stably cycle for 1,500 h without short circuits. Meanwhile, the LiFePO$_4$|LLZTO-600|Li full cell can retain 94.8% of its initial capacity after 150 cycles with the lowest overpotential among the SSEs. This work highlights the importance of tuning compaction pressure in developing high-performance SSEs and related SLBs.

Keywords: Compaction pressure, formation, garnet, solid-state electrolyte, solid-state lithium battery

INTRODUCTION

With the advancement and growing prominence of energy materials, numerous energy devices have been developed to satisfy the increasing demands of modern society. Solid-state lithium batteries (SLBs) that employ solid-state electrolytes (SSEs) are attractive due to their high energy density and enhanced safety compared to widely used lithium-ion batteries (LIBs)[1-5]. Among them, garnet-type $Li_7La_3Zr_2O_{12}$ (LLZO) SSEs and their derivatives are promising because of their high chemical stability[6] and wide electrochemical window[7-9], but the low compactness and inferior ionic conductivity of cubic-phase LLZO (c-LLZO) cannot meet the current practical requirements of SLBs.

Elemental doping is widely used to stabilize the phase structure by reducing Li content to induce Li vacancies, thus increasing the ionic conductivity of LLZO SSEs. The main doping methods include Li-site[10-13], La-site[14,15], Zr-site[16-18], and multi-site[19-23] doping, and most reports focus on Zr-site doping. Ohta *et al.* found that the ionic conductivity of LLZO is increased to 8×10^{-4} S cm^{-1} when the Nb^{5+} content is 0.25 per formula unit (pfu)[16]. Thompson *et al.* prepared the Ta-doped LLZO through a hot pressing method, and obtained the highest compactness of ~97% and the highest ionic conductivity when the lithium vacancy number is 0.5 ($Li_{6.5}La_3Zr_{1.5}Ta_{0.5}O_{12}$, LLZTO)[17]. Mukhopadhyay *et al.* calculated the Li-O bond lengths for different Ta-doping samples, showing that the Li-O bonds of LLZTO are longer than the other samples to facilitate faster Li$^+$ migration and higher ionic conductivity[18]. As a result, LLZTO stands out among various electrolytes due to its superior overall properties.

High-temperature sintering is the most critical step for densifying the LLZO pellets, including atmospheric sintering[24], hot pressing[25], electric-field assisted sintering[26], and plasma sintering[27]. Atmospheric sintering enables the mass production of LLZO pellets but is hindered by issues such as non-uniform sintering and material waste. In contrast, methods such as hot pressing, electric-field assisted sintering, and plasma sintering are effective for producing high-quality ceramics, but are not widely adopted due to their complex equipment requirements and high costs. For the widely used atmospheric sintering method, it has been reported that compaction pressure (before sintering) greatly influences the ceramic quality of sulfide electrolytes[28,29]. However, specific studies on oxide SSEs, particularly garnet-based SLBs, remain lacking.

In this work, the LLZTO pellets are compacted under different pressures and then sintered at 1,250 °C for 4 h (LLZTO-*x*, where *x* is the compaction pressure, MPa). The compacted LLZTO pellets show different morphologies and compositions, and the impact of compaction pressure on the performance of garnet-based SLBs is investigated. Among the samples, the Li|LLZTO-600|Li symmetric cell and $LiFePO_4$ (LFP)| LLZTO-600|Li full cell both exhibit the best performance, which is ascribed to the dense structure and restrained lithium loss upon sintering. This work elucidates the influence of compaction pressure on the formation and properties of LLZTO pellets, which could inspire the development of analogous SSEs and SLBs.

EXPERIMENTAL
Materials preparation

The LLZTO SSEs were prepared using a solid-state synthesis. The Li_2CO_3, La_2O_3, ZrO_2, and Ta_2O_5 precursors were weighed according to the stoichiometry of LLZTO, and 15% excess Li_2CO_3 was weighed to supplement the Li loss upon high-temperature synthesis. Subsequently, 20 g precursor, 40 g Zr beads, and 30 mL ethanol were added into the ball mill jars, which were placed in a high-energy ball miller (8000D, Spex SamplePrep, USA) and kept at 8,000 r min^{-1} for 1 h. The mixed powders were transferred to a vacuum oven set at 80 °C and heated for 12 h. The powders were ground after drying, and sintered in a muffle

furnace at 950 °C for 10 h with a heating rate of 2 °C min^{-1}. After natural cooling, the ground pre-sintered powders were placed into a mold and pressed under the pressure of 50, 150, 300 and 600 MPa. The compacted pellets were then heated at 1,250 °C for 4 h with a heating rate of 5 °C min^{-1}, and the LLZTO pellets were obtained after natural cooling.

Materials characterization

The crystal structure was analyzed using an X-ray diffraction (XRD) instrument (D8-A25, Bruker AXS, Germany) with Cu Kα radiation. The morphology and element distribution were examined by a scanning electron microscope (SEM) (SU-70, Hitachi, Japan) equipped with an energy dispersive spectroscopy (EDS) detector. The elemental composition and valence states were measured using an X-ray photoelectron spectroscopy (XPS) equipment (Escalab Xi+, Thermo Fisher, USA).

Electrochemical measurements

To measure the ionic and electronic conductivity, the Ag slurry was evenly sprayed on both sides of the polished LLZTO pellet. After drying, the Ag|LLZTO|Ag symmetric cells were tested on an electrochemical workstation (PARSTAT 3000A, Princeton, USA). The electrochemical impedance spectrum (EIS) plots were recorded with an amplitude potential of 10 mV and a frequency range of 10^6 to 10^{-1} Hz. The applied voltage of the steady-state current measurement was 200 mV. The LLZTO pellets were polished in an Ar-filled glove box (H_2O < 0.01 ppm and O_2 < 0.01 ppm) to assemble the Li|LLZTO|Li symmetric cells. To improve the interface contact, a drop (~10 μL) of liquid electrolyte containing 1M lithium hexafluorophosphate ($LiPF_6$) dissolved in ethylene carbonate/ethyl methyl carbonate/dimethyl carbonate (EC/EMC/DMC) (1:1:1 by volume) was applied to both sides of the LLZTO pellets. No solid electrolyte was added to the LFP cathode, but the above trace amount of liquid electrolyte was used to ensure good contact between LLZTO and LFP. The LFP|LLZTO|Li full cells were assembled in similar steps as the symmetric cells. To prepare the cathode sheets, LFP, polyvinylidene fluoride (PVDF), and acetylene black (8:1:1 by mass) were dissolved in N-methyl pyrrolidone (NMP) to form the slurry, which was then cast on aluminum foils and vacuum-dried at 85 °C for 12 h. The electrodes were cut into circle sheets with a diameter of 12 mm, and the mass loading of each sheet was ~1.5 mg. All electrochemical tests were performed at room temperature except for the activation energy tests.

RESULTS AND DISCUSSION

Figure 1A shows the XRD patterns of the different LLZTO pellets after sintering. It can be seen that all the characteristic peaks of each sample match well with the c-LLZO, and no Li-deficient-phase impurity $La_2Zr_2O_7$ (at ~28°-29°) is observed. Compared with the standard c-LLZO, the peaks of the samples shift to higher angles because the radius of Ta^{5+} is smaller than that of Zr^{4+}, and the lattice constant becomes smaller after the replacement of Zr^{4+} by Ta^{5+}. Since the peaks of $Li_7La_3Ta_2O_{13}$ are close to those of c-LLZO, each sample shows different degrees of peak splitting in the range of 30°-60° representing the $Li_7La_3Ta_2O_{13}$. As compaction pressure increases, the characteristic peaks and the peak splitting are more obvious, indicating the more $Li_7La_3Ta_2O_{13}$ and the higher crystallinity of SSEs. As shown in Figure 1B, the calculated grain size and micro-strain along the (422) facet are compared quantitatively. As compaction pressure rises, the grain size first increases and then decreases, while the micro-strain decreases and then increases. This indicates that higher compaction pressure leads to greater deformation, smaller particles, and denser structure.

Despite the similar sintering conditions, obvious morphology differences can be observed between the LLZTO pellets. For the LLZTO-50 pellet [Figure 1C], numerous pores are present in the worm-like structure due to insufficient contact between grains. For the LLZTO-150 pellet [Figure 1D], the grains are in contact with each other but are not completely densified, resulting in irregular hexagonal particles due to
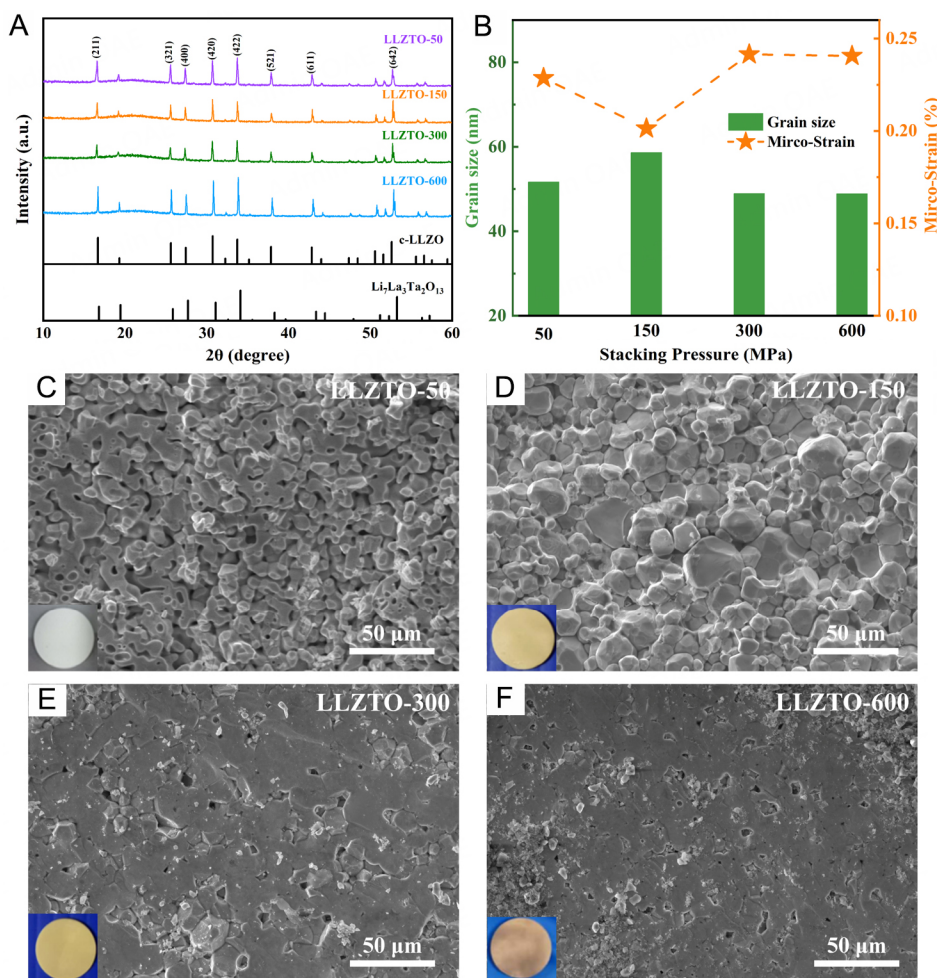
Figure 1. (A) XRD patterns of various LLZTO pellets. (B) Calculated grain size and micro-strain of various LLZTO pellets. Cross-section SEM images and related optical photos of (C) LLZTO-50, (D) LLZTO-150, (E) LLZTO-300, and (F) LLZTO-600 pellets.

the incomplete sintering of the grains. For the LLZTO-300 pellet [Figure 1E], the grains have close contact with each other, and the ceramic is thoroughly densified after sintering. Most of the grain boundaries disappear due to the complete fusion of grains, leaving only a few small pores. For the LLZTO-600 pellet [Figure 1F], the tight contact between grains leads to the densest morphology with absent grain boundaries and few pores.

Based on the energy difference and peak intensity of La 3d peaks of the LLZTO-50 [Figure 2A], the La elements primarily exist in a form similar to metal oxides. The Ta 4f peaks of LLZTO-50 consist of splitting peaks [Figure 2B], indicating the dominance of Ta^{3+} oxides. In contrast, the Ta 4f peaks of LLZTO-600 shift to higher binding energy, implying greater oxidation of Ta in the high-pressure pellets. Similarly, the Zr 3d peaks of LLZTO-600 also shift to higher binding energy [Figure 2C], suggesting a higher valence of Zr in the high-pressure pellets. The Li 1s peak of LLZTO-50 and LLZTO-600 [Figure 2D] are similar, except for the larger peak area in LLZTO-600, indicating reduced Li loss and complete sintering in high-pressure pellets. These results imply that higher compactness may lead to concentrated oxygen, promoting the stable oxidation of transition metals and increased Li content in SSEs.
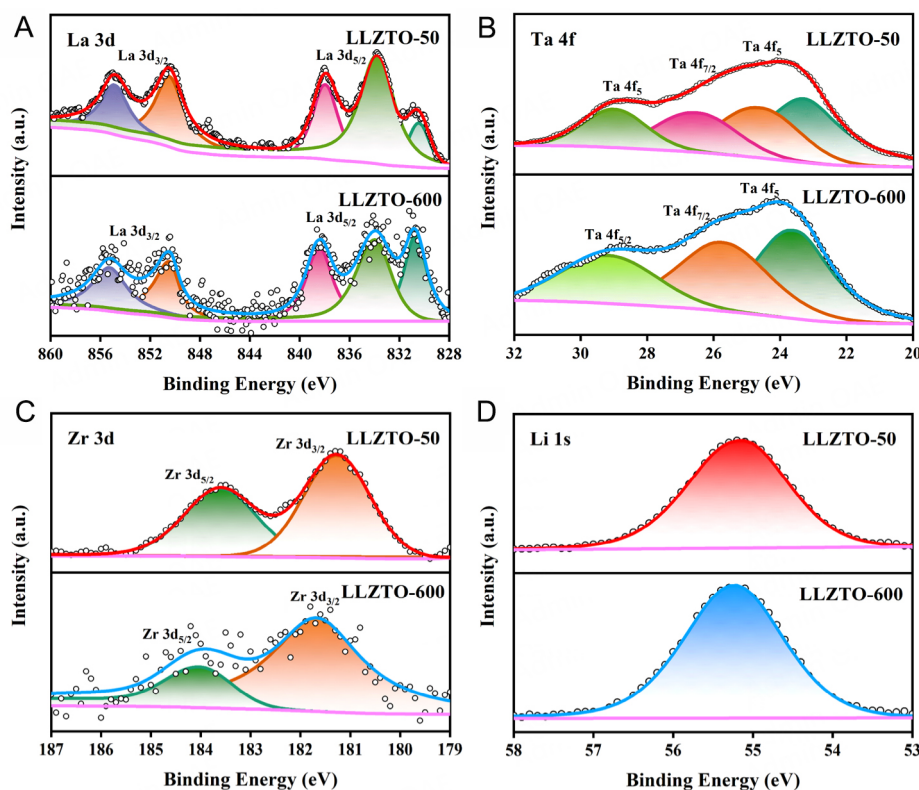
Figure 2. (A) La 3d, (B) Ta 4f, (C) Zr 3d, (D) Li 1s XPS peaks of LLZTO-50 and LLZTO-600 pellets.

The compactness increases with compaction pressure due to the improved contact between particles [Table 1]. All the EIS plots of the symmetric cells [Figure 3A and B] show a semicircle contributed by grain boundary and a straight line related to ionic diffusion. The total resistances of LLZTO-50, LLZTO-150, LLZTO-300, and LLZTO-600 are 53,150, 580, 450, and 366 Ω, respectively, and the calculated ionic conductivity [Table 1] is positively correlated with the compaction pressure. According to the calculated slopes derived from Figure 3C, the activation energy of LLZTO-50 is higher than the other samples due to more pores and insufficient contact between particles. When the polarization voltage is applied to the Ag|LLZTO|Ag symmetric cells [Figure 3D], the steady-state currents of LLZTO-50, LLZTO-150, LLZTO-300, and LLZTO-600 are 10, 18, 20, and 47 nA, respectively. The highest electronic conductivity [Table 1] of the LLZTO-600 pellet implies that it may not withstand high currents during repeated Li deposition. Critical current density (CCD) refers to the maximum current density that Li-Li symmetric cells can withstand to resist Li dendrite growth. As shown in Figure 3E, the CCDs of LLZTO-150, LLZTO-300, and LLZTO-600 are 0.34, 0.70, and 0.56 mA cm^{-2}, respectively. Consequently, despite the higher compactness of LLZTO-600, the higher electronic conductivity leads to a lower CCD compared to that of LLZTO-300. However, the ionic conductivity and CCD obtained in this work are also superior compared with the reported results[11,30-37] [Figure 3F]. In summary, the LLZTO-600 pellet has the highest ionic conductivity and favorable CCD among the samples, suggesting its potential application in high-performance SLBs.

The assembled Li|LLZTO|Li symmetric cells are used for galvanostatic charge/discharge tests to compare the interfacial stability of different samples to lithium metal. The initial polarization voltage of Li|LLZTO-150|Li is ~120 mV [Figure 4A], and it gradually increases at a uniform rate (~0.12 mV per cycle). The short circuit occurs after 487 cycles, and the polarization voltage drops from 180 to 50 mV, indicating that the Li

Table 1. Compactness, ionic conductivity, activation energy, and electronic conductivity of various LLZTO pellets

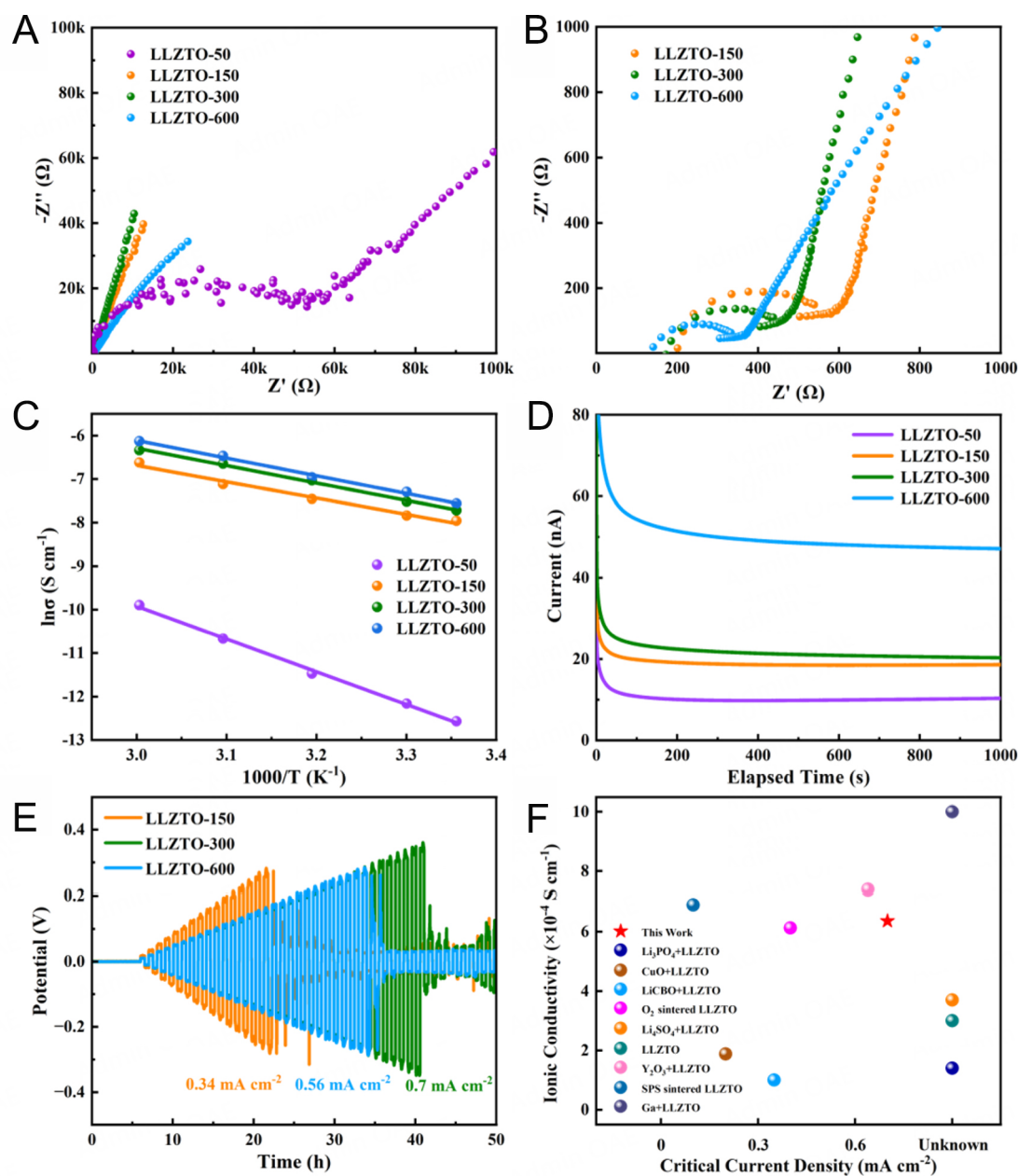| Compaction pressure (MPa)	50	150	300	600
Compactness (%)	61.08	88.88	91.58	94.00
Ionic conductivity (S cm^{-1})	1.63×10^{-6}	4.10×10^{-4}	5.30×10^{-4}	6.36×10^{-4}
Activation energy (eV)	0.65	0.32	0.34	0.35
Electronic conductivity (S cm^{-1})	5.77×10^{-9}	1.14×10^{-8}	1.36×10^{-8}	3.11×10^{-8}

Figure 3. (A) Overall and (B) Magnified EIS plots, (C) Arrhenius curves, and (D) Direct-current polarization curves of various Ag|LLZTO|Ag symmetric cells. (E) Critical current density (CCD) curves of various Li|LLZTO|Li symmetric cells. (F) Performance comparison of this work with the reported results[11,30-37].
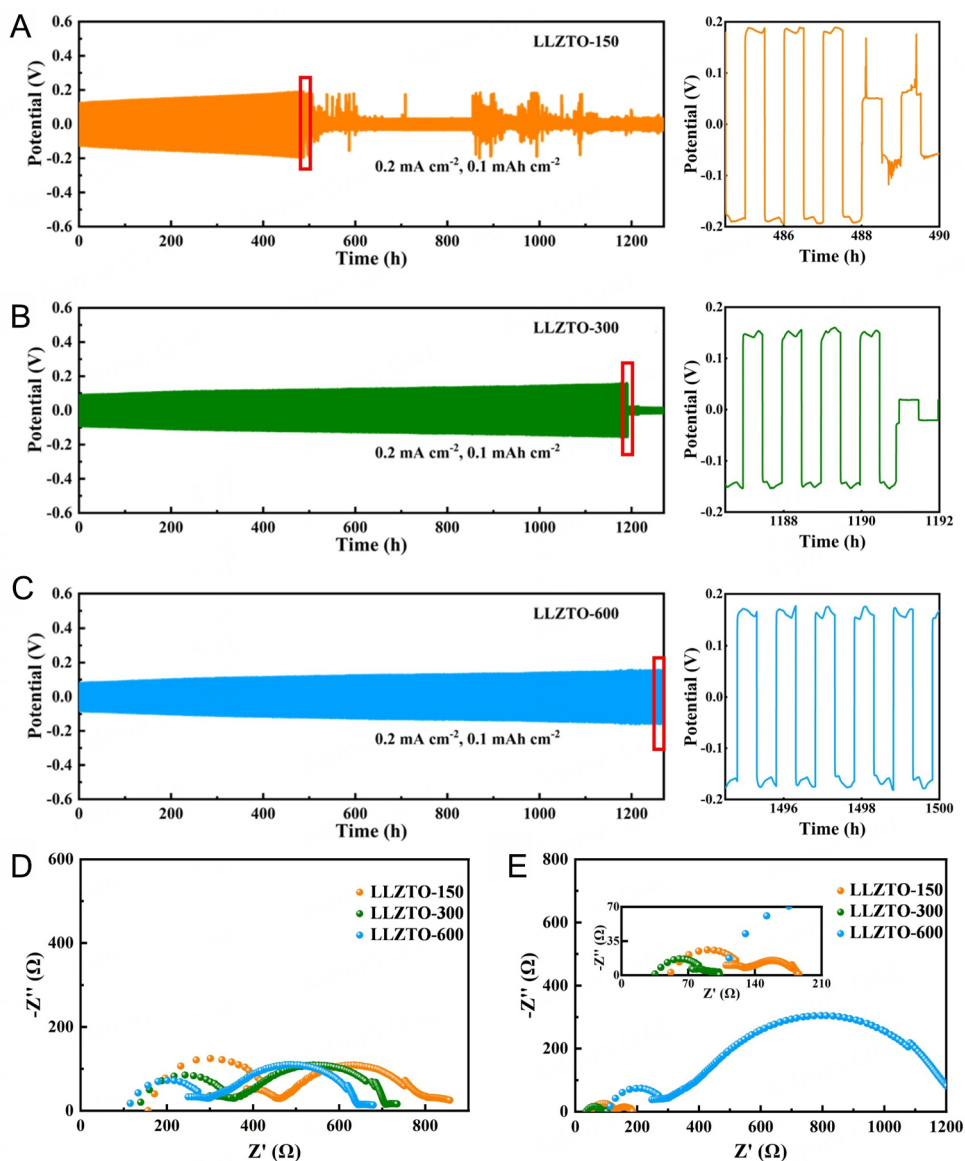
Figure 4. Cycling performance at various current densities of (A) LLZTO-150, (B) LLZTO-300, and (C) LLZTO-600 Li-symmetric cells. EIS of Li-symmetric cells (D) before cycling and (E) after 1,500 cycles.

dendrites start to grow along the grain boundary, resulting in a decrease in the "effective thickness" of the SSEs and a large decrease in the internal resistance of the cell. In the subsequent cycles, the polarization voltage stabilizes at 50 mV, exhibiting severe fluctuations up and down until the failure of the cell. Figure 4B shows the voltage-time curves of Li|LLZTO-300|Li, in which the initial polarization voltage is ~80 mV and the cells stably cycle at a current density of 0.2 mA cm^{-2} without voltage fluctuations. In the 1,190 cycles, the overpotential is stable only with an average increase of 0.06 mV per cycle, which is only half of that in Li|LLZTO-150|Li, indicating that the LLZTO-300 pellet has better stability to suppress Li dendrites. The Li|LLZTO-300|Li cells short-circuit at 1,191 cycles, and the voltage decreases from 150 to 20 mV, indicating that the Li dendrite growth has triggered a huge decrease in the internal resistance of the cell. As shown in Figure 4C, the Li|LLZTO-600|Li symmetric cell has the longest cycle life associated with the highest ionic conductivity and the largest compactness. The total resistances of LLZTO-150, LLZTO-300, and LLZTO-
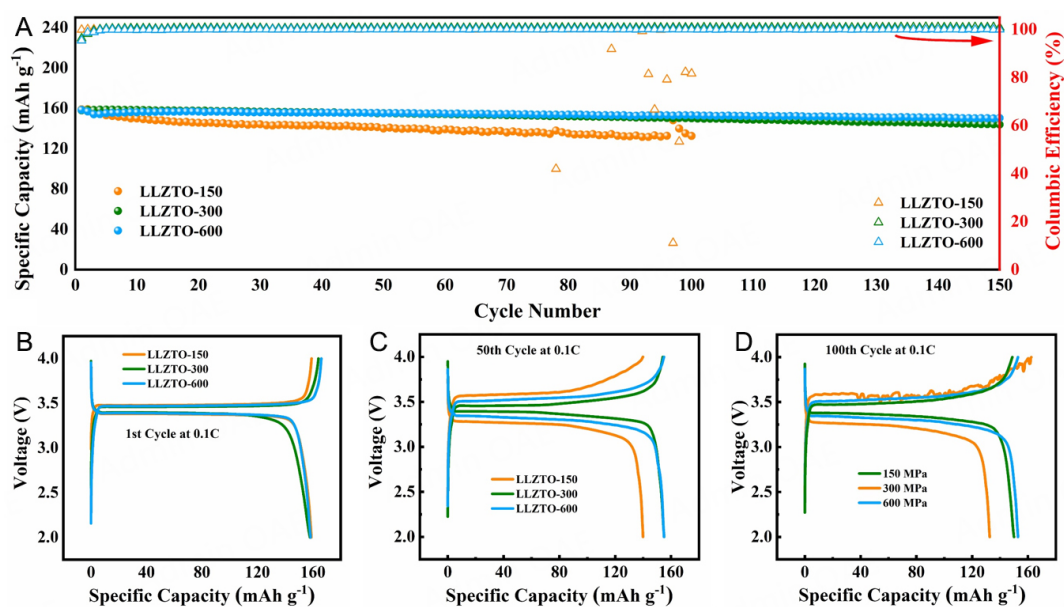
Figure 5. (A) Cycling performance and Coulombic efficiency of various LiFePO$_4$|LLZTO|Li full cells. (B-D) Corresponding 1st, 50th, and 100th charge/discharge curves at 0.1C.

600 Li-symmetric cells before cycling [Figure 4D] are 800, 700, and 640 Ω, respectively. The similar resistances indicate similar interfacial properties before cycling. After 1,500 cycles [Figure 4E], the LLZTO-150 and LLZTO-300 Li-symmetric cells exhibit small resistances (180 and 99 Ω) due to the short-circuit, while the total resistance of Li|LLZTO-600|Li is raised to 1,230 Ω caused by the interfacial degradation after cycling.

As shown in Figure 5A, the initial discharge capacity of LFP|LLZTO-150|Li [Figure 5B] is 158.9 mAh g^{-1}, and the initial Coulomb efficiency (CE) is as high as 99.9%. However, the capacity decays severely in the subsequent cycles. The overcharging occurs in the 78th cycle, and the capacity retention rate is only 83.4% after 100 cycles. The initial discharge capacity of LFP|LLZTO-300|Li [Figure 5B] is 157.9 mAh g^{-1}, and the initial CE is 96.3%. The reversible capacity remains at 143.8 mAh g^{-1} after 150 cycles, and the capacity retention rate is 91.1%. The initial discharge capacity of LFP|LLZTO-600|Li [Figure 5B] is 158.4 mAh g^{-1}, and the capacity retention rate after 150 cycles is 94.8%, which is the highest among all the full cells. This is because the highest ionic conductivity facilitates the stable Li$^+$ transport inside the cell, and the dense morphology facilitates stable cathode/electrolyte/anode interfaces. In the 50th cycle [Figure 5C], the LFP|LLZTO-150|Li cell exhibits the largest overpotential, even with severe voltage fluctuations in the 100th cycle [Figure 5D]. The stable voltage plateaus and the lowest overpotential of LFP|LLZTO-600|Li confirm the feasibility of enhancing the SLB performance by increasing the compaction pressure of SSEs.

CONCLUSIONS

In this paper, LLZTO pellets are prepared with different compaction pressures and sintered at 1,250 °C for 4 h showing various morphologies and compositions. The LLZTO-50 sample has a loose structure and lower metal valance states, while the LLZTO-600 sample demonstrates the largest compactness (94%) and the highest ionic conductivity (6.36 × 10^{-4} S cm^{-1}). As a result, the Li|LLZTO-600|Li symmetric cell exhibits the best performance, which can stably work for 1,500 cycles without short circuits. The reversible capacity of the LFP|LLZTO-600|Li full cell is 158.4 mAh g^{-1}, and the capacity retention rate is up to 94.8% after 150 cycles, which is the highest among the samples. In summary, the different compaction pressure can regulate

the composition and structural stability of SSEs, thus enhancing the electrochemical performance of garnet-based SLBs.

DECLARATIONS

Authors' contributions

Made substantial contributions to the conception and design of the study and performed data analysis and interpretation: Zhu, J.; Wu, Y.; Wang, L.; Lin, J.

Performed data acquisition: Zhu, J.; Wu, Y.; Zhang, H.; Xie, X.; Wang, L.; Lin, J.

Provided technical and material support: Yang, Y.; Peng, H.; Liang, X.; Qi, Q.; Lin, W.; Peng, D. L.

Wrote the first version of the manuscript: Zhu, J.; Wu, Y.; Lin, J.

All authors revised the manuscript.

Availability of data and materials

The data are available upon request from the authors.

Conflicts of interest

All authors declared that there are no conflicts of interest.

Ethical approval and consent to participate

Not applicable.

Consent for publication

Not applicable.

Copyright

REFERENCES

1. Zhu, Y.; He, X.; Mo, Y. Origin of outstanding stability in the lithium solid electrolyte materials: insights from thermodynamic analyses based on first-principles calculations. *ACS. Appl. Mater. Interfaces.* **2015**, *7*, 23685-93. DOI PubMed

2. Diederichsen, K. M.; Mcshane, E. J.; Mccloskey, B. D. Promising routes to a high Li^+ transference number electrolyte for lithium ion batteries. *ACS. Energy. Lett.* **2017**, *2*, 2563-75. DOI

3. Li, J.; Ma, C.; Chi, M.; Liang, C.; Dudney, N. J. Solid electrolyte: the key for high-voltage lithium batteries. *Adv. Energy. Mater.* **2015**, *5*, 1401408. DOI

4. Takada, K. Progress in solid electrolytes toward realizing solid-state lithium batteries. *J. Power. Sources.* **2018**, *394*, 74-85. DOI

5. Fuller, T. F.; Doyle, M.; Newman, J. Simulation and optimization of the dual lithium ion insertion cell. *J. Electrochem. Soc.* **1994**, *141*, 1. DOI

6. Wu, J. F.; Pang, W. K.; Peterson, V. K.; Wei, L.; Guo, X. Garnet-type fast Li-ion conductors with high ionic conductivities for all-solid-state batteries. *ACS. Appl. Mater. Interfaces.* **2017**, *9*, 12461-8. DOI

7. Jia, L.; Zhu, J.; Zhang, X.; Guo, B.; Du, Y.; Zhuang, X. Li-solid electrolyte interfaces/interphases in all-solid-state Li batteries. *Electrochem. Energy. Rev.* **2024**, *7*, 12. DOI

8. Li, B.; Chao, Y.; Li, M.; et al. A review of solid electrolyte interphase (SEI) and dendrite formation in lithium batteries. *Electrochem. Energy. Rev.* **2023**, *6*, 7. DOI

9. Zhang, J.; Wang, C.; Zheng, M.; et al. Rational design of air-stable and intact anode-electrolyte interface for garnet-type solid-state batteries. *Nano. Energy.* **2022**, *102*, 107672. DOI

10. Rettenwander, D.; Blaha, P.; Laskowski, R.; et al. DFT study of the role of Al^{3+} in the fast ion-conductor $Li_{7-3x}Al^{3+x}La_3Zr_2O_{12}$ garnet. *Chem. Mater.* **2014**, *26*, 2617-23. DOI PubMed PMC

11. El-Shinawi, H.; Paterson, G. W.; Maclaren, D. A.; Cussen, E. J.; Corr, S. A. Low-temperature densification of Al-doped $Li_7La_3Zr_2O_{12}$: a reliable and controllable synthesis of fast-ion conducting garnets. *J. Mater. Chem. A.* **2017**, *5*, 319-29. DOI

12. Wagner, R.; Redhammer, G. J.; Rettenwander, D.; et al. Fast Li-ion-conducting garnet-related $Li_{7-3x}Fe_xLa_3Zr_2O_{12}$ with uncommon $I\bar{4}3d$ structure. *Chem. Mater.* **2016**, *28*, 5943-51. DOI PubMed PMC

13. Wu, J. F.; Chen, E. Y.; Yu, Y.; et al. Gallium-Doped $Li_7La_3Zr_2O_{12}$ garnet-type electrolytes with high lithium-ion conductivity. *ACS. Appl. Mater. Interfaces.* **2017**, *9*, 1542-52. DOI

14. Deviannapoorani, C.; Shankar, L. S.; Ramakumar, S.; Murugan, R. Investigation on lithium ion conductivity and structural stability of yttrium-substituted $Li_7La_3Zr_2O_{12}$. *Ionics* **2016**, *22*, 1281-9. DOI

15. Rangasamy, E.; Wolfenstine, J.; Allen, J.; Sakamoto, J. The effect of 24c-site (A) cation substitution on the tetragonal-cubic phase transition in $Li_{7-x}La_{3-x}A_xZr_2O_{12}$ garnet-based ceramic electrolyte. *J. Power. Sources.* **2013**, *230*, 261-6. DOI

16. Ohta, S.; Kobayashi, T.; Asaoka, T. High lithium ionic conductivity in the garnet-type oxide $Li_{7-x}La_3(Zr_{2-x}, Nb_x)O_{12}$ (x=0-2). *J. Power. Sources.* **2011**, *196*, 3342-5. DOI

17. Thompson, T.; Sharafi, A.; Johannes, M. D.; et al. A tale of two sites: on defining the carrier concentration in garnet-based ionic conductors for advanced Li batteries. *Adv. Energy. Mater.* **2015**, *5*, 1500096. DOI

18. Mukhopadhyay, S.; Thompson, T.; Sakamoto, J.; et al. Structure and stoichiometry in supervalent doped $Li_7La_3Zr_2O_{12}$. *Chem. Mater.* **2015**, *27*, 3658-65. DOI

19. Dhivya, L.; Murugan, R. Effect of simultaneous substitution of Y and Ta on the stabilization of cubic phase, microstructure, and Li^+ conductivity of $Li_7La_3Zr_2O_{12}$ lithium garnet. *ACS. Appl. Mater. Interfaces.* **2014**, *6*, 17606-15. DOI

20. Inada, R.; Yasuda, S.; Tojo, M.; Tsuritani, K.; Tojo, T.; Sakurai, Y. Development of lithium-stuffed garnet-type oxide solid electrolytes with high ionic conductivity for application to all-solid-state batteries. *Front. Energy. Res.* **2016**, *4*, 28. DOI

21. Chen, C.; Sun, Y.; He, L.; et al. Microstructural and electrochemical properties of Al- and Ga-doped $Li_7La_3Zr_2O_{12}$ garnet solid electrolytes. *ACS. Appl. Energy. Mater.* **2020**, *3*, 4708-19. DOI

22. Cao, Z.; Cao, X.; Liu, X.; et al. Effect of Sb-Ba codoping on the ionic conductivity of $Li_7La_3Zr_2O_{12}$ ceramic. *Ceram. Int.* **2015**, *41*, 6232-6. DOI

23. Meesala, Y.; Liao, Y. K.; Jena, A.; et al. An efficient multi-doping strategy to enhance Li-ion conductivity in the garnet-type solid electrolyte $Li_7La_3Zr_2O_{12}$. *J. Mater. Chem. A.* **2019**, *7*, 8589-601. DOI

24. Murugan, R.; Thangadurai, V.; Weppner, W. Fast lithium ion conduction in garnet-type $Li_7La_3Zr_2O_{12}$. *Angew. Chem. Int. Ed.* **2007**, *46*, 7778-81. DOI PubMed

25. Zhang, J.; Li, J.; Zhai, H.; Tan, G.; Tang, X. One-step processing of soft electrolyte/metallic lithium interface for high-performance solid-state lithium batteries. *ACS. Appl. Energy. Mater.* **2020**, *3*, 6139-45. DOI

26. Ihrig, M.; Mishra, T. P.; Scheld, W. S.; et al. $Li_7La_3Zr_2O_{12}$ solid electrolyte sintered by the ultrafast high-temperature method. *J. Eur. Ceram. Soc.* **2021**, *41*, 6075-9. DOI

27. Zhu, Y.; Zhang, J.; Li, W.; Xue, Y.; Yang, J.; Li, S. Realization of superior ionic conductivity by manipulating the atomic rearrangement in Al-doped $Li_7La_3Zr_2O_{12}$. *Ceram. Int.* **2023**, *49*, 10462-70. DOI

28. Cronau, M.; Szabo, M.; König, C.; Wassermann, T. B.; Roling, B. How to measure a reliable ionic conductivity? The stack pressure dilemma of microcrystalline sulfide-based solid electrolytes. *ACS. Energy. Lett.* **2021**, *6*, 3072-7. DOI

29. Lee, C.; Han, S. Y.; Lewis, J. A.; et al. Stack pressure measurements to probe the evolution of the lithium-solid-state electrolyte interface. *ACS. Energy. Lett.* **2021**, *6*, 3261-9. DOI

30. Hosokawa, H.; Takeda, A.; Inada, R.; Sakurai, Y. Tolerance for Li dendrite penetration in Ta-doped $Li_7La_3Zr_2O_{12}$ solid electrolytes sintered with $Li_{2.3}C_{0.7}B_{0.3}O_3$ additive. *Mater. Lett.* **2020**, *279*, 128481. DOI

31. Janani, N.; Ramakumar, S.; Kannan, S.; Murugan, R. Optimization of lithium content and sintering aid for maximized Li^+ conductivity and density in Ta-doped $Li_7La_3Zr_2O_{12}$. *J. Am. Ceram. Soc.* **2015**, *98*, 2039-46. DOI

32. Ni, K. H.; Chen, Z. L.; Li, C. C. Densification and stress distribution within the sintered structure of ceramic electrolytes for all-solid-state Li-ion batteries. *Acta. Mater.* **2024**, *275*, 120057. DOI

33. Shen, F.; Guo, W.; Zeng, D.; et al. A simple and highly efficient method toward high-density garnet-type LLZTO solid-state electrolyte. *ACS. Appl. Mater. Interfaces.* **2020**, *12*, 30313-9. DOI

34. Xu, B.; Li, W.; Duan, H.; et al. Li_3PO_4-added garnet-type $Li_{6.5}La_3Zr_{1.5}Ta_{0.5}O_{12}$ for Li-dendrite suppression. *J. Power. Sources.* **2017**, *354*, 68-73. DOI

35. Yamada, H.; Ito, T.; Hongahally, B. R. Sintering mechanisms of high-performance garnet-type solid electrolyte densified by spark plasma sintering. *Electrochim. Acta.* **2016**, *222*, 648-56. DOI

36. Zhang, H.; Wu, Y.; Zhu, J.; et al. Fusing Ta-doped $Li_7La_3Zr_2O_{12}$ grains using nanoscale Y_2O_3 sintering aids for high-performance solid-state lithium batteries. *Nanoscale* **2024**, *16*, 14871-8. DOI

37. Zhang, W.; Sun, C. Effects of CuO on the microstructure and electrochemical properties of garnet-type $Li_{6.3}La_3Zr_{1.65}W_{0.35}O_{12}$ solid electrolyte. *J. Phys. Chem. Solids.* **2019**, *135*, 109080. DOI